ACS OMEGA

http://pubs.acs.org/journal/acsodf

Article

Toward Continuous Breath Monitoring on a Mobile Phone Using a Frugal Conducting Cloth-Based Smart Mask

Pillalamarri Srikrishnarka, Raaga Madhuri Dasi, Sourav Kanti Jana, Tripti Ahuja, Jenifer Shantha Kumar, Ankit Nagar, Amoghavarsha Ramachandra Kini, Boby George,* and Thalappil Pradeep*

Cite This: *ACS Omega* 2022, 7, 42926−42938

Read Online

ACCESS | Metrics & More | Article Recommendations | Supporting Information

ABSTRACT: A frugal humidity sensor that can detect changes in the humidity of exhaled breath of individuals has been fabricated. The sensor comprises a humidity-sensitive conducting polymer that is *in situ* formed on a cloth that acts as a substrate. Interdigitated silver electrodes were screen-printed on the modified cloth, and conducting threads connected the electrodes to the measurement circuit. The sensor's response to changing humidity was measured as a voltage drop across the sensor using a microcontroller. The sensor was capable of discerning between fast, normal, and slow breathing based on the response time. A response time of ∼1.3 s was observed for fast breathing. An Android-based mobile application was designed to collect sensor data *via* Bluetooth for analysis. A time series classification algorithm was implemented to analyze patterns in breathing. The sensor was later stitched onto a face mask, transforming it into a smart mask that can monitor changes in the breathing pattern at work, play, and sleep.

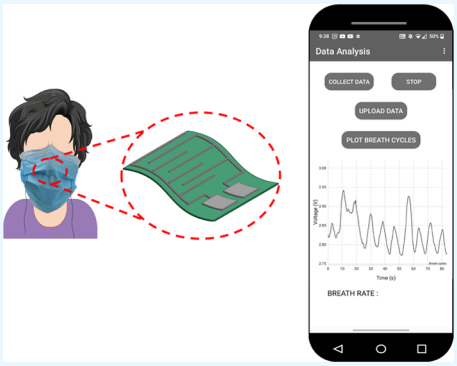

INTRODUCTION

With ever growing concerns pertaining to the health and environmental impact caused by air pollution across the globe, a quick, affordable and noninvasive health monitoring device is the need of the hour. A recent investigation of the disease burden in 2017 revealed that ∼544.9 million people suffer from chronic respiratory diseases globally.[1] Monitoring humidity is crucial in many industries including those of food processing, semiconductor manufacturing, packaging, agriculture, and medicine.[2−4] Respiration is vital to sustaining human life, and the exhaled breath is a treasure trove that contains a vast variety of components such as water vapor, carbon dioxide, and volatile organic components, which can reveal vital information on health.[5,6] Apart from analyzing these components, measurement of the tidal volume and breath rate assists in determining the physiological state of the individual. A humidity sensor that is flexible, fast-responsive, affordable, and mobile phone-enabled can be deployed for continuous monitoring of breath rate and can eventually help determine the status of health.

In this regard, there have been advances toward fabricating humidity sensors that are capable of detecting humidity levels in exhaled breath. Typically, sensing is achieved by measuring with various transducing methods, including capacitance,[7,8] resistance,[9,10] absorbance,[11−13] surface acoustic waves,[14−17] and adsorption on quartz crystal microbalance,[18−21] and by devices such as a field effect transistor.[22,23] A variety of materials including conducting polymers, metal oxides, noble metal nanoparticles, carbon nanotubes, and graphene oxide have been investigated for their humidity-sensing capabilities. A humidity sensor reported by Mogera et al. showed a response time of ∼10 ms, which is one of the fastest responding supramolecular systems.[20,24,25] Yi et al. fabricated an optical fiber-based humidity sensor that utilized a microknot resonator incorporated into a Mach−Zehnder (MZ) interferometer and observed a response time of 84 ms. Although these sensors possess quick response times, their major drawbacks are high cost and complicated fabrication methods.[10] Textiles and paper-based substrates have paved the way for flexible/wearable electronics, especially sensors and nanogenerators. These are ideal as they are robust, nontoxic, high in availability, affordable, and have easy processability. Whitesides and colleagues first fabricated a paper-based flexible humidity sensor having digitally printed graphite electrodes on a piece of paper that was attached to a surgical mask.[26] Duan et al. further simplified the fabrication process of humidity sensors by utilizing a conducting polyester tape on a regular printing paper to detect changes in the exhaled breath.[27] Cellulose was chosen as an ideal substrate for humidity sensing as it offers ease in chemical modification, thus making it conducive for large-scale sensor fabrication.[28−32] A highly porous paper-

Received: August 6, 2022
Accepted: September 15, 2022
Published: November 16, 2022

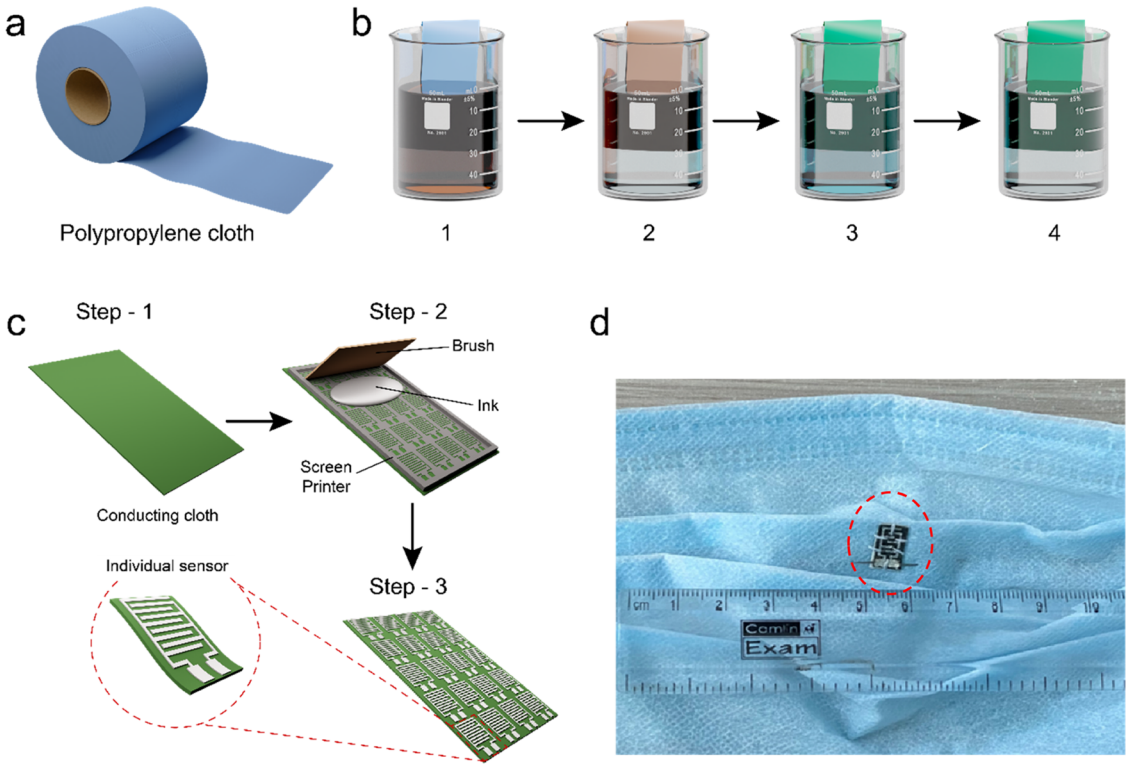

Figure 1. Schematic representation of the sensor fabrication process. (a) Roll of polypropylene (PP) mat. (b) SILAR procedure where a small piece of PP was immersed in beaker 1 containing aniline in HCl (aq). The mat was subsequently transferred to beaker 2 containing DI water. From this beaker, it was further immersed in beaker (3), which contained 12 g of APS in 1 M HCl (in water). Finally, the mat was rinsed in beaker (4) containing DI water, wherein its color changed from blue to green. (c) The dried conducting cloth was stretched on a frame for screen printing. The interdigitated electrode template was placed on top of the conducting cloth upon which silver paste was spread as shown in step 3. Finally, the sensor array cloth was dried, from which individual sensors were trimmed. A magnified view of a single sensor is shown in the dashed circle. (d) The sensor stitched on a common surgical mask. The sensor is marked with a circle.

based humidity sensor was fabricated by treating the copy paper with hydrochloric acid to remove calcium carbonate and washing to create porous structures.[33] After electrodes were screen-printed, the time periods for response and recovery were 0.8 and 0.78 s, respectively.[33] Recently, Chen and co-workers fabricated a flexible paper-based humidity sensor using origami, and conducting polyester electrodes were assembled onto the paper substrate that was folded along a predesigned pattern. They obtained a response and recovery time of 155 and 58 s, respectively, and their sensor was sensitive in a large humidity range.[34] A similar response and recovery time were observed from a carbon ink-coated filter paper-based humidity sensor.[35] Additionally, this sensor was self-powered and delivered an output voltage of 0.19 V and was highly flexible for ∼1000 bends.[35] However, due to the fragile nature of the paper, under continuous breathing, the paper could potentially become moist and subject to tare under stress. This could render the sensor difficult to use.

On the other hand, textiles are far more robust, flexible, and easy to process, thus making them ideal substrates for wearable electronics.[36−38] Wang et al. deposited graphene oxide (GO) on a bovine serum albumin (BSA)-coated nonwoven cloth by soaking the cloth in GO suspension and transforming it into a resistance-based humidity sensor. This sensor noted an average response of ∼8.9 s and a recovery of ∼11.6 s.[39] Recently, Allison et al. coated a commercially available cotton cloth with p-doped conjugated poly(3,4 ethylenedioxythiophene)/chloride *via* chemical vapor deposition. Integrating this modified cotton on a face mask enabled the user to freely move, and the sensor was capable of differentiating different breathing patterns such as shallow and deep.[40] Wu and co-workers designed a flexible humidity sensor capable of respiration monitoring by creating interdigitated electrodes based on silver nanowires as the ink on a flexible leather cloth. Leather was chosen as it is biocompatible, low-cost, and convenient.[41] Recently, metal-organic frameworks (MOFs) have been investigated for their various sensing capabilities. In this aspect, Rauf et al. reported a smart textile containing a MOF film grown using the Langmuir−Blodgett (LB) technique resulting in a sensor capable of detecting water vapor in the presence of several volatile organic compounds.[42] Recently, Bokka et al. fabricated a water-soluble MoSSe quantum dots/poly(vinyl alcohol) (PVA) film as a humidity sensor that was capable of discerning different breathing patterns.[43] The breathing data were analyzed using a neural network algorithm for classifying them into different breathing patterns. Liu et al. recently fabricated a fabric-based humidity sensor using a hydrophobic-hydrophilic patterned polyester-spandex fabric as a substrate that was subsequently treated with polydopamine-acid carbon nanotubes (aCNTs) that were quick and sensitive to a large humidity range.[44] They observed a quick response and recovery time of 0.46 and 0.56 s, respectively.

Although there have been many humidity sensors with fast response time, ease of fabrication, and good sensitivity, they are not economical due to expensive raw materials, longer processing steps, or the requirement of complex electronic circuitry. From our previous work, we observed that conducting polymers such as polyaniline (PANi) can be *in*

https://doi.org/10.1021/acsomega.2c05017
ACS Omega 2022, 7, 42926−42938

situ polymerized on electrospun nanofibers of poly(vinylidene fluoride) (PVDF) by successive ionic layer adsorption and reaction (SILAR).[45] It is a versatile technique with upscaling capabilities due to its simplicity. We used SILAR for *in situ* polymerization of PANi on various substrates. This modified cloth was capable of sensing the changes in breath humidity over extended periods with a response time of ∼0.31 s. This was integrated into a face mask that transformed it into a smart mask. Conversion of the smart mask as a personal health monitoring and evaluation device integrated into a mobile phone is also presented.

EXPERIMENTAL METHODS

Materials. Commercially available nonwoven polypropylene (PP) cloth and woven cotton, silk, and polyester cloth were procured locally. Aniline and ammonium persulfate (APS) were from RANKEM India. Hydrochloric acid was from Sigma Aldrich. Ethanol, lithium chloride (LiCl), magnesium chloride ($MgCl_2$), potassium carbonate (K_2CO_3), magnesium nitrate ($MgNO_3$), sodium bromide (NaBr), sodium chloride (NaCl), and potassium chloride (KCl) were from Alfa Aesar. Millipore-produced deionized water (∼18 MΩ) was used throughout the experiment, and all of the chemicals were used as received without further purification unless mentioned otherwise.

Methods. *Fabrication of the Conducting PP Cloth.* From a roll of nonwoven PP fabric shown in Figure 1a, a small cloth of 12 cm × 12 cm dimension was cut and soaked in water for 12 h to ensure complete wetting; this is a vital step to ensure complete coverage of PANi. About 6 mL of aniline and 12 g of APS were added to two different beakers containing 80 mL of 1 M aqueous HCl solution. This wet cloth was later immersed in aniline solution for 5 min (Figure 1b1) and subsequently transferred to another beaker containing clean water to remove any unbound aniline molecules (Figure 1b2). Further, the cloth was soaked in a beaker containing APS for 10 min (Figure 1b3). The cloth was finally transferred into another beaker containing deionized (DI) water, as shown in Figure 1b4. This cycle was repeated 17 times for the growth of PANi on the mat (Figure 1). The cloth was later dried at 75 °C for 12 h for further use. Due to the growth of polyaniline on the cloth, the blue cloth was transformed to green. Interdigitated electrodes, with a gap of 0.6 mm, were screen-printed on the sensor *via* screen printing with commercial grade Ag paste. Upon drying of the ink, the cloth was cut into individual sensor elements for further analysis.

Electrochemical Analysis of the Sensor. The sensor element was taped to a glass slide for support, and electrical contacts were made with silver paste on the screen-printed silver pads. The other ends of the contact wires were connected to a Palmsense Emstat electrochemical workstation. An input bias potential of 3 V was provided to the sensor, and the chronoamperometric response in the presence of humidity was noted. All of the experiments were performed at 45 ± 5% relative humidity (RH) and 25 °C, recorded using standard sensors. Exhaled air through the nose and mouth was directly pointed toward the sensors for sensing changes in humidity. A commercially available Eurolab plastic thermos-hygrometer was used to measure humidity.

A detailed description of the sensor unit is given in the Supporting Information. All of the components necessary for the measurement are presented in Table S3.

Fabrication of a Prototype Smart Mask. From the conducting mat with interdigitated electrodes printed on it, an individual sensor of size 6 mm × 12 mm was cut and stitched onto a surgical mask. The sensor was placed almost at the center of the mask, where the flux of the exhaled breath was maximum. The region was selected such that it is not interfered with by any creases and is directly exposed to exhaled breath. Stainless steel conducting threads were used to connect the sensor to a microcontroller. The conducting thread and sensor were coupled using silver paste (Electrolube Silver conducting paint) and kept for drying. The schematic of the controller is shown in Figure S6. A detailed cost analysis for different components used for the sensor is given in Table S3.

Smart Mask Deployment. A sample size of 23 volunteers was selected who were in the age range of 21−58, of which 14 were male and 9 were female. An average body mass index (BMI) of 24.2 ± 4.8 for the interest group was noted. They were asked to exhale orally and through the nose to determine the breathing pattern and test the sensors' versatility in discerning different breathing patterns. Furthermore, the volunteers were asked to periodically cough for 5 s and breath for 10 s for a total period of 120 s so as to artificially introduce noise into the breathing pattern. Similarly, the subjects were asked to periodically withhold breathing for 10 s and breath for 10 s for a total of 120 s. These breathing data were used to train a deep neural network and several other classification algorithms for identifying the breathing frequency and to differentiate between normal and abnormal breathing.

Characterization. To investigate the size and morphology of bare and PANi-coated PP mat, they were characterized using a Thermo Scientific Verios U4 GHC field-emission scanning electron microscope (FESEM) with a retractable detector operating at 2 kV. The samples were sputter-coated with gold using a CRESSINGTON sputter-coater for 120 s. To understand the conformation of organic functional groups anchored on the fibers, infrared (IR) spectra were collected using a Perkin Elmer Spectrum One Fourier-transform infrared spectroscopy (FTIR) in the attenuated total reflection (ATR) mode. Raman spectral analysis was performed using a WiTec GmbH confocal Raman microscope (α-300 s). A laser with a wavelength of 532 nm neodymium-doped yttrium aluminum garnet (Nd−YAG), with an excitation power of 0.2−0.5 mW, was maintained throughout the experiment. A 100× objective lens was used for visualizing the fibers. Time-lapse Raman spectra were collected by placing the sensor under the objective, and oral breath was exhaled on the sensor. Spectra were collected for 50 s, with a time interval of 1 s. Impedance spectroscopy was performed on the sensor using a Biologic CH electrochemical workstation. The spectrum was collected using an alternating current (AC) signal of 20 mV with a direct current (DC) potential of 2 V. The frequency of the AC signal was varied between 7 MHz and 9 Hz, and the subsequent change in the impedance spectrum was noted. Contact angle measurements were performed using a Holmarc contact angle meter with a 3 μL sessile water droplet. Then, 3 × 3 cm^2 bare and PANi-treated PP mats were placed on a glass slide, which in turn were brought under the droplet for calculating the water contact angle.

RESULTS AND DISCUSSION

For the fabrication of a flexible, wearable sensor, nonwoven PP cloth was chosen as the substrate. It possesses structural

https://doi.org/10.1021/acsomega.2c05017
ACS Omega 2022, 7, 42926−42938

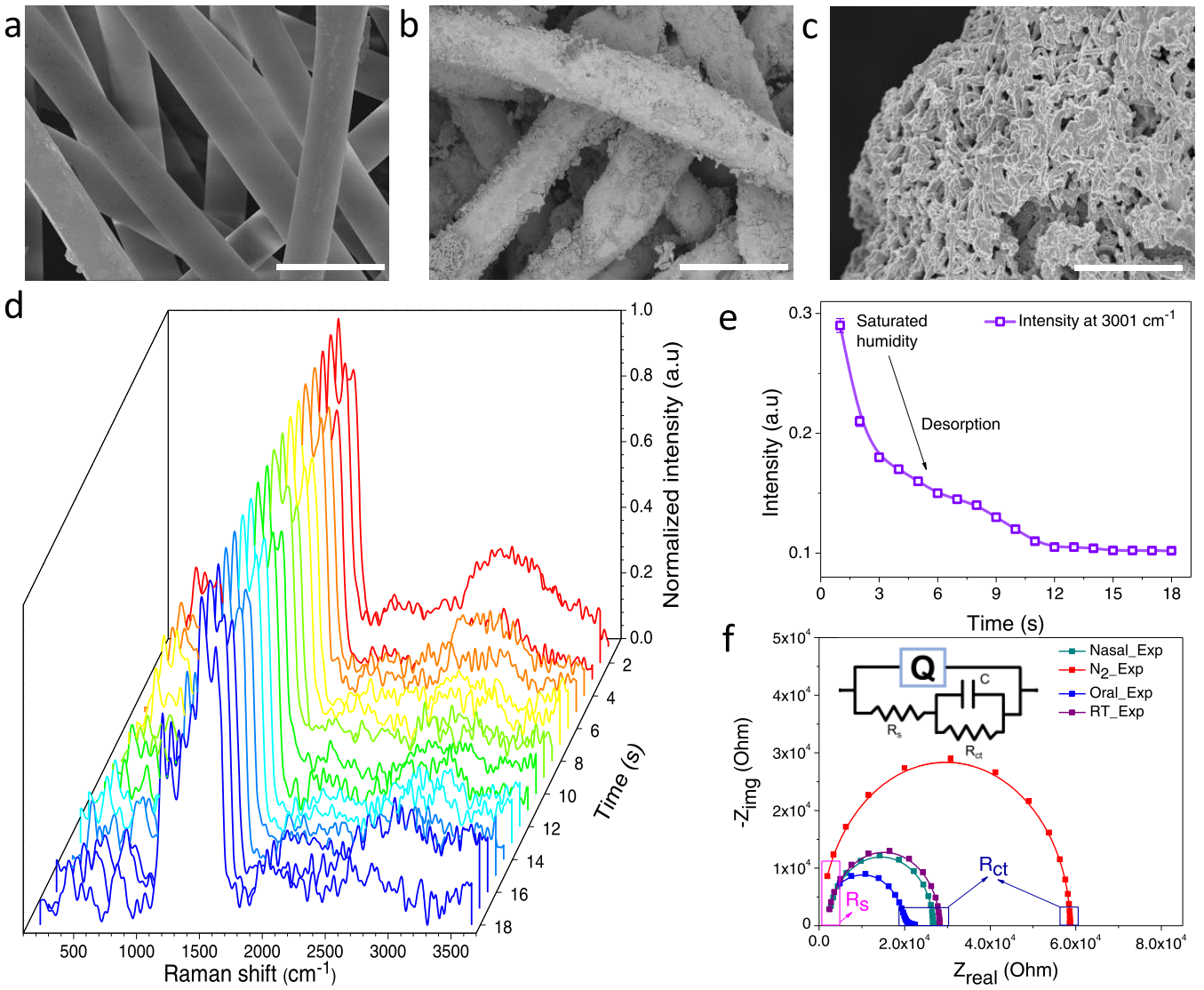

Figure 2. Scanning electron micrographs of (a) bare PP and (b, c) PANi-coated PP (scale bar is 50 μm for (a, b) and 1 μm for (c), respectively). (d) Time-dependent Raman spectra for understanding water desorption. (e) Variation in intensity for the peak at 3001 cm^{-1}. (f) Nyquist plot to determine the R_s and R_{ct} of the sensor at room temperature and in dry air and nasal and oral breath exhalation. The circuit arrangement used for fitting the Nyquist plot is shown in the inset.

integrity against multiple bending cycles and offers high flexibility and the least resistance to the passage of air. A schematic representation of the fabrication process is depicted in Figure 1 (details are provided in the Materials and Methods Sections). Upon performing SILAR, the color of the mat changed from blue to green.

To visualize the morphological changes occurring during SILAR treatment, high-resolution scanning electron micrographs were collected for both bare and PANi-coated PP mats (Figure 2a–c). Fibers of the PP mat were randomly arranged, and their surfaces appeared smooth. The fibers were uniform in diameter (~20 μm), as observed in Figure 2a. Upon SILAR, aniline was polymerized on the PP fibers as evident from the deposits, making the surface of the fibers extremely rough as seen in Figure 2b. These structures are highly porous in nature (Figure 2c), which could assist in enhancing the sensitivity.

To confirm the presence of PANi on PP, FTIR and Raman spectroscopic analyses were performed, and the corresponding results are shown in Figure S1. FTIR spectra of untreated and PANi-coated PP are shown in Figure S1a. All of the characteristic peaks were assigned and are listed in Table S2. Peaks at 1245, 1303, and 3203 cm^{-1} for the PANi-coated PP mat were assigned to γ(C–N), aromatic γ(C–N), and γ(N–H) stretching, respectively, thereby confirming the presence of PANi. A comparative study of the vibrational features of both bare and PANi-coated PP mats was performed using Raman spectroscopy (Figure S1b). The black trace represents bare PP, and the red trace represents a PANi-coated mat. A summary of these results is presented in Table S3.

To understand the adsorption–desorption dynamics of water molecules from the sensor, a time-dependent Raman spectral analysis on the cloth was performed. The conducting cloth was saturated with humidity by continuous exposure to exhaled breath, and time-lapse Raman spectra were collected for 18 s, at an interval of 1 s, as shown in Figure 2d. A broad peak at ~3001 cm^{-1} is attributed to the grouped frequencies of C–H and N–H, as observed in our previous work.[45] We believe that there could be a hydrogen bond between $-(NH)^+$ of PANi and H_2O, which assists in proton hopping. The peak intensity at 3001 cm^{-1} reduced as the water molecule desorbed

https://doi.org/10.1021/acsomega.2c05017
ACS Omega 2022, 7, 42926–42938

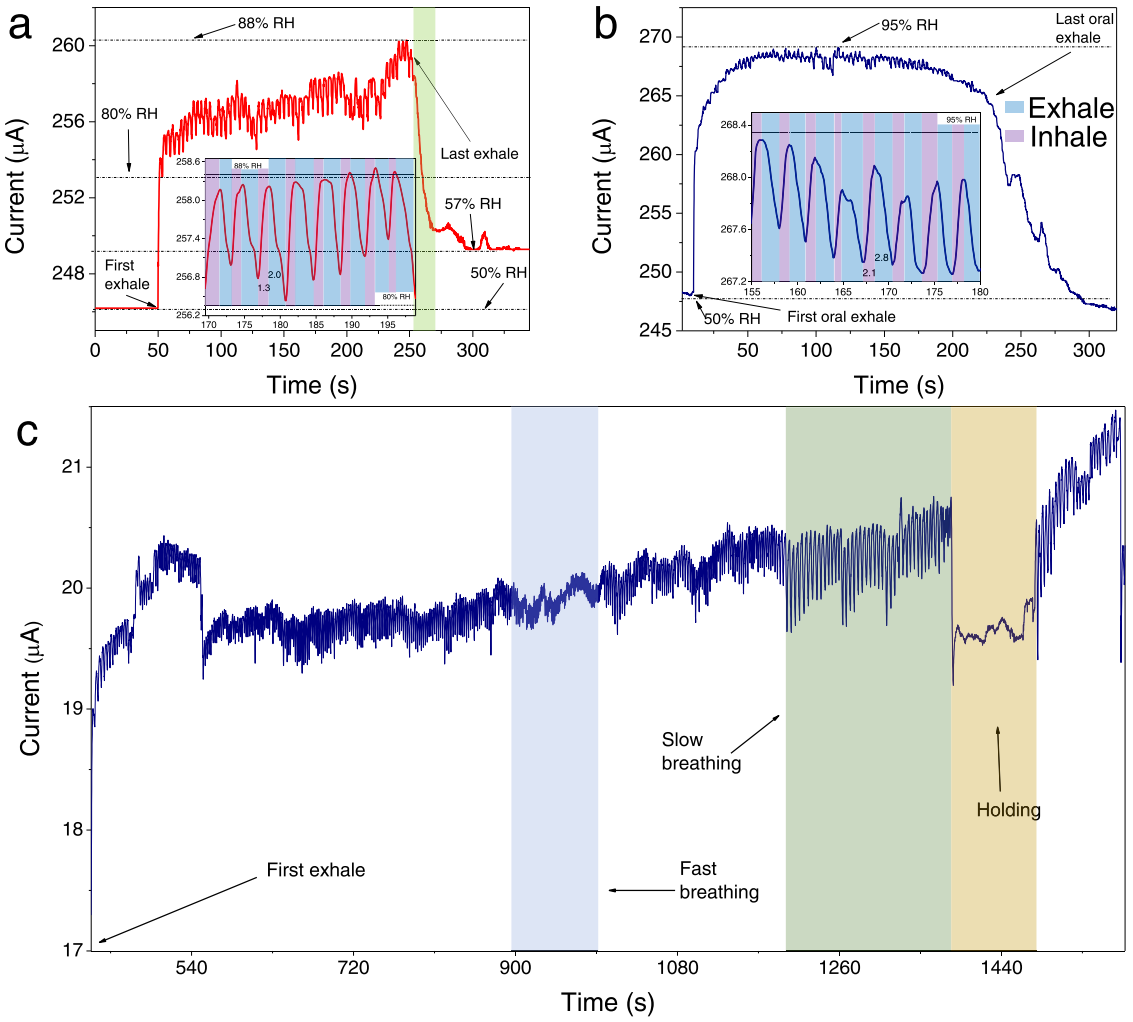

Figure 3. Chronoamperometric analysis for (a) nasal and (b) oral breath. Insets show magnified regions for understanding the response and recovery time. (c) Response of the sensor stitched on a surgical mask to nasal breathing over a longer period under various breathing styles (fast breathing, slow breathing, and holding). The data in (a, b) were measured using copper leads, while that in (c) were measured using the conducting thread.

from the surface of PANi. The intensity was plotted as a function of time (Figure 2e). The intensity dropped instantaneously within 1 s, reducing by ∼27.7%, and continued to drop as time progressed. The intensity stabilized after ∼12 s, indicating complete desorption of water molecules from the surface.

We further performed impedance spectroscopy to elucidate the mechanism of the sensing element under varying humidity. The Nyquist plots obtained in each case are shown in Figure 2f. Each Nyquist spectrum has two intercepts to the X axis, the first intercept corresponds to the surface resistance (R_s) of the sensing material. The second intercept represents a change in the resistance (R_{ct}), which is related to proton hopping caused by the adsorption/desorption of water molecules from the surface. In Nyquist spectra, R_s is not clearly seen, as it was not possible to measure the impedance beyond 7 MHz due to the limitation of the electrochemical analyzer.

The impedance of our sensor was measured by maintaining dry-air conditions by purging N_2 over the sensor (Figure 2f). The corresponding R_{ct} decreased from 58 to 26 kΩ, which is a result of the adsorption of ambient water molecules on the surface of the mat. Upon nasal exhalation on the sensor, the resistance decreased to 24 kΩ and was further reduced to ∼21.9 kΩ upon oral exhalation. This reduction in R_{ct} was attributed to the increased adsorption of water molecules in a high-humidity atmosphere, which results in increased proton hopping between the two contact pads. The capacitance of the sensor was 0.87×10^{-12} F under the dry-air condition and increased to 0.94×10^{-12} F under the room-temperature condition. Upon nasal exhalation, the capacitance increased to 3.4×10^{-12} F, and in the presence of oral exhalation, it reached 22×10^{-12} F. This increase in capacitances could be due to the formation of a capacitive double layer due to the spontaneous adsorption of moisture on the surface. The electronic circuit used to fit each Nyquist spectrum is shown in the inset in Figure 2f. The values have been tabulated and shown in Table S4.

An ideal sensor must possess a quick response and recovery time, which is possible if the sensor has an affinity toward water molecules and simultaneously undergoes fast desorption. To achieve these, the surface of the sensor should be ambiphilic in nature. To understand the wetting property of the sensor surface, the water contact angle before and after PANi coating was measured (Figure S2). The results suggested that the PP mat is hydrophobic in nature as the contact angle was 143° (Figure S2a). After growing PANi on the mat, the

https://doi.org/10.1021/acsomega.2c05017
ACS Omega 2022, 7, 42926−42938

Scheme 1. Schematic Representation of the Sensing Mechanism. (a) Adsorption of H_2O on PANi, (b) Proton Transfer between the Partially Protonated PANi Backbone and H_2O, and (c) Desorption of Water Molecules after Proton Transfer

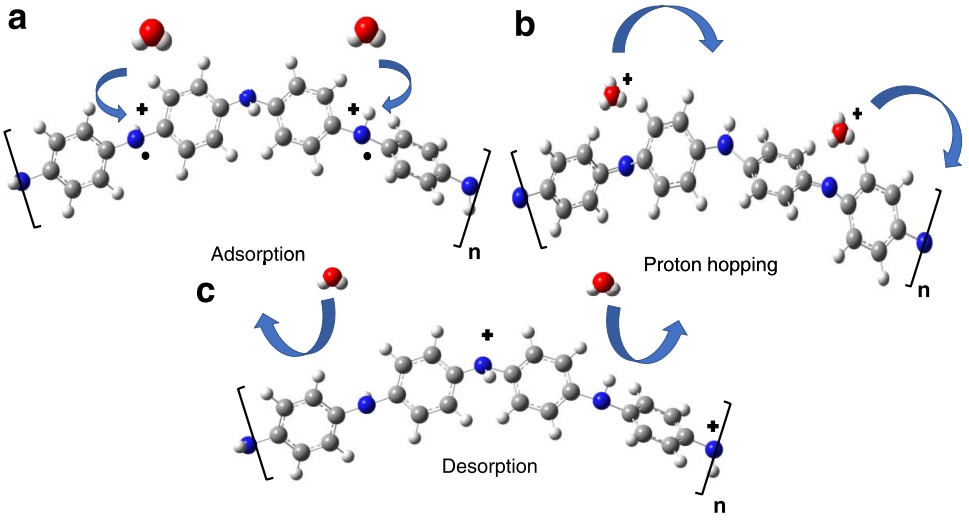

contact angle reduced to 120°, which suggested that the mat lost its hydrophobic nature slightly, as seen in Figure S2b. We believe that due to this complex behavior, quick response and recovery are observed.

Chronoamperometric Response of the Sensor. To study the performance of the sensor under oral and nasal exhaled breath, the sensor was connected to a PalmSens electrochemical workstation, and a chronoamperometric study was performed with an applied external voltage of 3 V to the sensor. Subsequently, the current was measured under different breathing conditions, as shown in Figure 3. The sensor was initially allowed to stabilize at room temperature for 50 s, after which the first nasal exhalation was performed. As a result, the current rose from 246 to 256 μA as shown in Figure 3a. It took ∼13 s for humidity to desorb completely from the surface of the sensor, as marked in the green box in Figure 3a. It is evident that the sensor is versatile in determining inhalation and exhalation (Figure 3a inset). We observed a response time of ∼1.3 ± 0.19 s and a recovery time of ∼2.07 ± 0.32 s. The sensor was further subjected to oral exhalation, and the resulting chronoamperometric analysis is shown in Figure 3b. Upon first oral exhalation, the current rose by 17 μA. Oral inhalation and exhalation were continued further for 200 s. From the sensing results, it is evident that the time required for the desorption of water molecules from the surface of the sensor is ∼65 s. However, in the case of oral exhalation, the sensor was capable of distinguishing both with a response time of ∼2.1 ± 0.23 s and a recovery time of ∼2.8 ± 0.31 s (Figure 3b inset).

Further, to collect real-time data by conducting field trials using facemasks, the sensor was stitched to a mask. Since copper wires do not stitch well, they were replaced with conducting threads and silver paste. A chronoamperometric study was then performed to determine the sensor response (Figure 3c). The sensor was capable of discerning different breathing patterns. Upon the first exhalation, a rise of 3 μA was recorded, and the peaks were present clearly even after continuous breathing. Initially, the volunteer was asked to breathe normally for a period of 420 s. The time period for a cycle of inhalation and exhalation was ∼2.4 ± 0.5 s. For a period of ∼2 min (from 900 to 1020 s), the volunteer performed fast breathing. During this period, the inhalation−exhalation cycles lasted for ∼1.2 s with a breath rate of ∼82 breaths/min. Subsequently, the volunteer was asked to execute deep inhalation and slow exhalation. In this regime, the time period for one breath cycle was ∼4.4 ± 0.3 s. Finally, at the end of 1380 s, upon the last exhalation, the volunteer was asked to hold his/her breath for a period of ∼60 s, after which the breathing continued. We observed a slight increase in the overall current as time progressed. This could be attributed to the increased adsorption of moisture on the sensor during the breath-holding time.

The exhaled breath comprised several different compounds. An analysis of these compounds would relate to understanding the well-being of an individual. Acetone and ethanol are some of the commonly known components of exhaled breath in diabetics[46] and alcoholics,[47] respectively. Droplets containing different concentrations of an ethanol−water mixture were brought close to the sensor, and the response from the sensor was recorded (Figure S3a). As the concentration of ethanol increased, the drop in current also increased. A plot of concentration vs current shows the drop (Figure S3b). Similarly, the sensor's response in the presence of acetone−water mixture is shown in Figure S3c. A plot depicting a drop in current vs concentration of acetone is shown in Figure S3d. The drop was the highest for pure ethanol compared to acetone; however, at 5% concentration in water, there was a gain in current in the case of ethanol, unlike acetone. An increase in water content in the droplet results in a decrease in the current drop, which suggests that the sensing mechanism is based on Grotthuss proton hopping. In pure droplets of acetone and water, in the absence of H_2O molecules, no H_3O^+ species are observed, which is necessary for proton hopping. As the concentration of water in each of the droplets increases, the overall current drop also reduces. As soon as the droplet of acetone or ethanol is brought near the vicinity of the sensor, due to their high vapor pressure, the vapors of these volatile molecules disperse the adsorbed moisture on the sensor, and in the absence of protons on the surface of the sensor, a dip in the conductivity is observed with a drop in current. In the case of binary mixtures, due to the lower surface tension of ethanol/acetone within the droplet, these molecules tend to move toward the surface of the water droplet.[48] From the surface, the vapors of acetone/ethanol evaporate and they disperse the

https://doi.org/10.1021/acsomega.2c05017
ACS Omega 2022, 7, 42926−42938

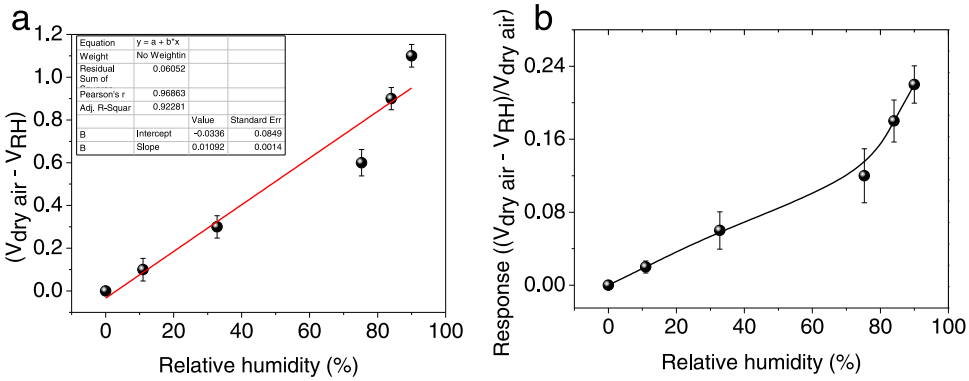

Figure 4. (a) Difference between the output voltage and the output voltage at different relative humidity conditions vs % relative humidity. (b) Sensor's response at different % RH values.

Figure 5. (a) Photograph of a volunteer wearing the mask. (b) Screen grabs of the Android application designed to monitor the breathing pattern. (c) Breathing patterns of a volunteer recorded using the mobile application depicting normal breathing.

adsorbed water molecules on the surface of the sensor. We suspect that as the concentrations of these volatile species decrease inside the droplet, the overall vapor pressure reduces, resulting in a decrease in the current drop. When a drop of the water−ethanol mixture (95% water, 5% ethanol) was brought close to the surface of the sensor, there was an increase in the current, which reduced as the droplet was retracted from the surface. We suspect that as the ethanol molecules evaporated from the droplet, a small number of water molecules might have evaporated along with them. With the increase of protons on the surface of the sensor, the conductivity might have increased.

Sensing Mechanism. We believe that the Grotthuss proton hopping is the underlying mechanism of sensing.[49] Adsorption of H_2O molecules on the surface of PANi is driven by the formation of intermolecular hydrogen bonds as shown in Scheme 1a. This acts as a "switch" throughout the surface, resulting in an increase in the conductivity with an increase in the ambient %RH levels. The Emeraldine salt form of PANi in a partially protonated state enables it to form a "switch" in the

https://doi.org/10.1021/acsomega.2c05017
ACS Omega 2022, 7, 42926−42938

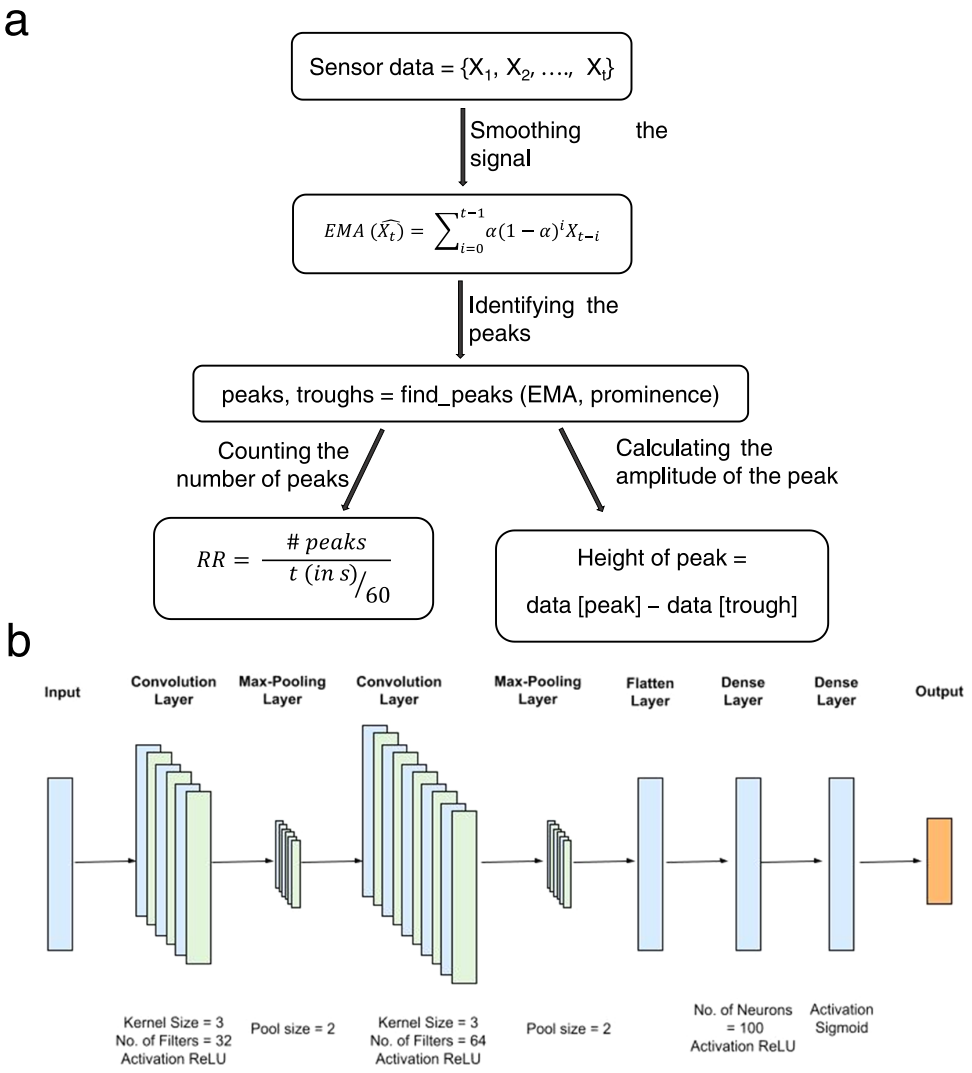

Figure 6. (a) Flow chart describing the process of obtaining the respiration rate (RR). (b) 1D convolutional neural network used for binary classification.

presence of the adsorbed water molecules. This results in the formation of H_3O^+ intermediary species, which are then transferred to the neighboring nitrogen atom as shown in Scheme 1b. Finally, desorption of the H_2O species occurs due to the hydrophobic nature of the PP backbone (Scheme 1c).

Antibacterial Activity. Due to the close vicinity of the sensor to the mouth, there is a possibility of bacterial growth on the sensor. To understand the bacterial inhibition property of the sensor, untreated PP and PANi-coated PP were placed on agar plates inoculated with Gram-negative (*Escherichia coli*) and Gram-positive (*Bacillus subtilis*) bacteria. Fresh bacterial cultures of *E. coli* (MTCC 443), *E. coli* (MTCC 739), and *B. subtilis* were spread on nutrient agar plates along with ∼1 cm × 1 cm pieces of the mats placed on top. Digital photographs of the agar plate containing the sensors with the bacterial lawn are shown in Figure S4. After overnight incubation at 37 °C, the bacterial lawn formed was observed to not interact with PP and PANi-coated PP along its boundaries. This was confirmed through a thin, observable zone of inhibition along PP, though it was not prominent in the latter.

Calibration of the Sensor. The sensor's response under different controlled humidity conditions was measured as shown in Figure S5. Supersaturated salt solutions were used to control humidity inside a bottle. A plot of $(V_{\text{dry air}} - V_{\text{RH}})$ vs % RH is shown in Figure 4a; the slope of this curve shows the sensitivity of the sensor. The calibration curve depicting the response of the sensor in different humidity conditions is shown in Figure 4b. Details pertaining to the amount of salt used are given in Table S1.

Design and Assembly of a Real-Time Monitoring Sensor through a Mobile Application. The sensor unit after calibration was stitched on a disposable surgical mask, and a conducting thread was used to connect the mask to the prototype board (Figure S6). The components needed for the circuitry along with the cost of each component are provided in Table S5. All of the procured components were commercially available, and their overall cost can be further reduced with scale. A volunteer was requested to wear the modified surgical mask and breathe on the sensor (Figure 5a). An Android mobile application was developed to record the readings and record the number of breath cycles. The screen grabs from the application are shown in Figure 5b. Upon opening the application, the user is directed to the home page that directly leads to the "Find devices tab," where the user selects the available device. Thereafter, the user profile details are recorded. The user can then start measuring the breath

https://doi.org/10.1021/acsomega.2c05017
ACS Omega 2022, 7, 42926−42938

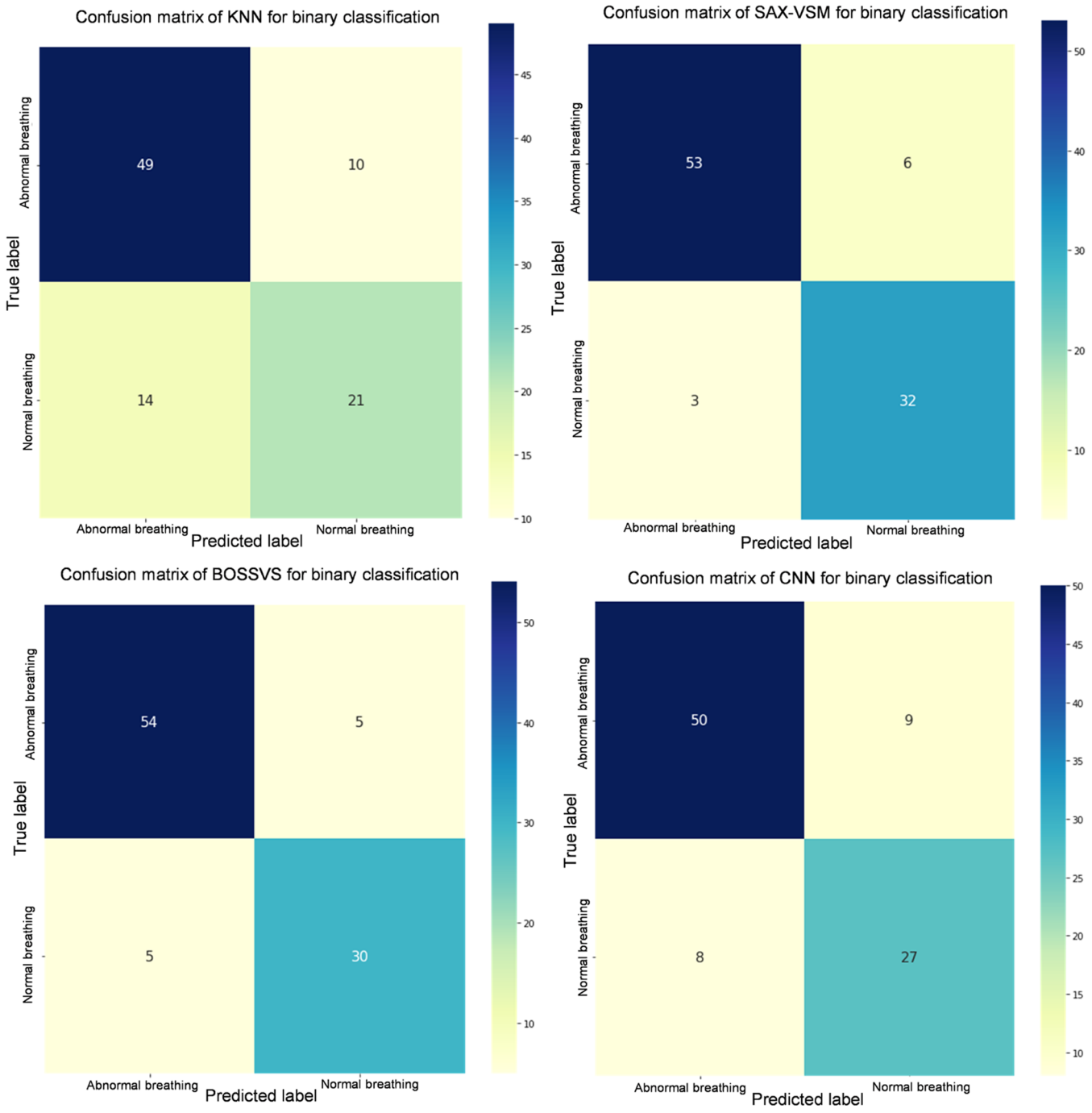

Figure 7. Comparing the performance of different classifiers on the collected data.

data. Once he/she is satisfied with the duration of breathing, the user can upload the data or directly plot the data, which gives the breath rate. The data obtained can be stored in their personal drive for future analysis. The responses obtained from the microcontroller in the presence of different breathing patterns are plotted in Figure S7.

Unlike in the case of the chronoamperometric study, wherein exhalation resulted in a rise in the current, the output voltage across the sensor decreased. We suspect this to be due to the increased capacitive nature of the sensor in the presence of humidity. Sensitivity is presented as the ratio of output voltage under dry air conditions to output voltage under exhalation. The time taken for one breath cycle was ∼5.1 s, as the volunteer was asked to breathe normally. From Figure S7a,b, the breathing frequency of 13 and 6 breaths per min were observed for normal and slow breathing, respectively. As soon as the volunteer exhaled onto the sensor, an increase in the sensitivity was observed, which took ∼2.89 s to reach the maximum. Subsequently, as soon as the volunteer started to inhale, the sensitivity decreased (Figure S7a). When the volunteer exhaled slowly through the nose, there was a gradual increase in the sensitivity. The individual needed ∼10.3 s for one exhalation−inhalation cycle. This rise and fall in sensitivity is almost synchronous to the normal breathing rate of the individual. The breathing response of six different volunteers is shown in Figure S8. The sensor was able to differentiate

https://doi.org/10.1021/acsomega.2c05017
ACS Omega 2022, 7, 42926−42938

between slow, normal, and fast breathing, as the amplitude and time period of each peak was different for each breathing pattern. The fast-breathing pattern had a smaller amplitude compared to that of the normal or slow pattern. For some volunteers, the relative humidity of the nasal breath and oral exhalation was ∼65 and ∼80%, respectively.

Sleep apnea is a serious sleeping disorder in which, due to irregular breathing, sleep is often disturbed, leaving the patients tired. The sensor's capability to discern between breathing and breath holding was tested by asking a volunteer to breathe normally through the nose 5 times and hold the breath for 10 s. This cycle was repeated for a total duration of 120 s. The recorded response is shown in Figure S9. As soon as the volunteer began to hold his/her breath, a dip in the sensitivity was observed as humidity desorbed from the sensor. The response reversed as the volunteer followed up with a deep inhalation.

Furthermore, a volunteer was requested to wear the mask for an extended period while comfortably sitting and working on the laptop (Figure S10). While doing chores, no anomalies in the sensor's response were observed. An analysis of breath quality under stress for several volunteers falls under the scope of future work.

Categorization of Breathing Patterns. The flow from the collection of raw data to classification is shown in Figure 6a. Initial raw data were collected from Arduino Uno, from which exponentially weighted moving average (EMA), a smoothing technique, was applied to the time-ordered sequence of data. From the smoothed data, peaks and peak amplitude were calculated using the "find_peaks" function of the SciPy library. As shown in Figure 6b, a one-dimensional (1D) convolutional neural network with two convolutional layers and two fully connected layers was used, since neural networks are capable of automatically extracting features from time series. There was a max polling layer after every convolutional layer. The last layer performed the binary classification, and a sigmoid activation function was used. A binary cross-entropy loss function with the Adam optimizer was used. A batch size of 8 was selected, and the number of epochs was 50. These hyperparameters were chosen empirically.

The data collected from the smart mask were modeled as a time series since the humidity of exhaled breath varied with time. It was cleaned (filtered and smoothened) and split into segments of 1 min. A label was assigned to the segment based on the nature of breathing cycles in it. Segments with normal nasal and oral breathing were assigned the label "normal." Segments with deep nasal and oral breathing were assigned the label "slow." Segments with quick nasal and oral breathing were assigned the label "fast." A total of 373 segments were obtained from all of the volunteers with 139 for normal breathing, 136 for deep breathing, and 98 for quick breathing. These segments were then used to form the dataset for training the classification algorithms. The binary classification was implemented to classify the samples as normal and abnormal (fast and slow). The algorithm used logistic regression, 1D convolutional neural network (1D CNN), Bag-of-Symbolic Fourier Approximation (SFA) Symbols in Vector Space (BOSSVS), k-Nearest Neighbors (kNN), and Symbolic Aggregate approXimation in Vector Space Model (SAX-VSM) for classifying the breathing pattern. The performance metrics used were accuracy (Acc), true positive rate (TPR), and false positive rate (FPR), which are defined below. Abnormal breathing was assigned as positive and normal breathing as negative for evaluating the accuracy of each model.

$$\mathrm{Acc} = \frac{\mathrm{TP} + \mathrm{TN}}{\mathrm{TP} + \mathrm{TN} + \mathrm{FP} + \mathrm{FN}}$$

$$\mathrm{TPR} = \frac{\mathrm{TP}}{\mathrm{TP} + \mathrm{FN}}$$

$$\mathrm{FPR} = \frac{\mathrm{FP}}{\mathrm{FP} + \mathrm{TN}}$$

As concluded from Figure 7, an accuracy of 60.6% was observed for logistic regression, 81.91% for the 1D convolutional neural network, 89.36% for BOSSVS, and 74.46% for kNN, and the best accuracy of 90.42% was observed for SAX-VSM (Figure 7). These results have been tabulated in Table S6.

For studying the breathing pattern, smart masks were provided to 23 volunteers, and they were asked to exhale both orally and through the nasal passage. Some of their responses are shown in Figure S11. While wearing the masks, the volunteers were seated and were asked to breathe continuously for 120 s to calculate the time needed for slow breath, albeit oral or nasal. The time period was recorded to be 8.02 s, with outliers at 16.0 and 2.0 s. The longest time to take a complete breath, i.e., both inhalation and exhalation, was 16.0 s. On the other hand, the average time needed for a normal breath cycle was 3.2 s, the slowest being at 5.1 s and the fastest at 2.0 s for a complete breathing cycle. When the volunteers were asked to breathe faster, the average time was observed to be 1.8 s, and the slowest and fastest times were ∼2.9 and 1.1 s, respectively. Thus, the sensor showed dynamic sensing capability by being able to distinguish between slow, fast, and normal breathing patterns. We believe that the sensor can be worn for extended periods of time and the breathing data can be collected for detailed analysis.

A comparison of different humidity sensors that have been employed for breath monitoring is given in Table S7. The absence of exotic materials such as graphene, carbon nanotubes, quantum dots, and MoS_2, yet having almost a similar performance, makes our sensor compelling for everyday breath monitoring. SILAR is frugal and simplistic in fabrication and therefore can be fabricated by anyone with a basic understanding of the technique and can be further expanded to use other conducting polymers and applied on different fabric materials as well. We believe that due to its ease of fabrication and affordability, our sensor can be upscaled and deployed at a large scale for recording breathing patterns. The sensors were found to be extremely stable even after 1 year, although these sensors were fabricated in February 2020 and were tested during July−December 2021 due to multiple lockdowns. They were stable for long-term use. One of the volunteers wore the mask continuously for 120 min, and data were collected. Additionally, as the breathing data can be recorded on a mobile phone, the data can be shared with a specialist who could then analyze and provide appropriate suggestions on the medical condition. Furthermore, these data can be analyzed using a neural network algorithm for further improvement in the accuracy of the prediction.

A major challenge is device validation through clinical trials having larger datasets, which improves the accuracy of the models utilized. The electronic components used are the major

https://doi.org/10.1021/acsomega.2c05017
ACS Omega 2022, 7, 42926−42938

contributors to the price and the physical size of the device, which require optimization. Addressing these issues may help in providing everyone with a smart mask that is minimalistic, trendy, and affordable for everyday use.

CONCLUSIONS

A frugal humidity sensor was fabricated by *in situ* polymerization of aniline on nonwoven PP cloth using SILAR. The fabrication process is scalable and affordable, thereby making it conducive for large-scale manufacturing. The sensor was later stitched on a disposable surgical mask, thereby transforming it into a smart mask for continuous monitoring of changes in the exhaled breath. The sensor was also capable of detecting various concentrations of acetone and ethanol, thus making it versatile. Bacterial growth studies indicated that even though the zone of inhibition was limited, the growth over the sensor cloth was not observed, thus rendering it safe for prolonged use. An Android phone application was designed to collect and analyze the user's breathing pattern and categorize it into fast, slow, and normal regimes. Our scalable, versatile, and affordable sensor along with analytics can help analyze the health of people. Such smart masks could be used for daily breath monitoring in hospitals and during workouts.

ASSOCIATED CONTENT

Supporting Information

The Supporting Information is available free of charge at https://pubs.acs.org/doi/10.1021/acsomega.2c05017.

Volatile organic compound testing protocol; sensor fabrication process; 1D convolutional neural network; (BOSSVS) algorithm; (SAX-VSM) algorithm; (kNN) classifier; FTIR and Raman spectra of bare PP and PANi-coated PP mats; contact angle measurements of bare PP and PANi-coated PP; table containing the parameters obtained from the Nyquist plot; calibration curve of the sensor under various values of humidity; response of the sensor in the presence of ethanol and acetone; antibacterial response of the sensor; fabrication of the sensor and the circuit diagram of the sensor assembly; breathing response of various volunteers; table containing the bill of materials; breathing response of a volunteer while performing various activities; performance of the various classification algorithms used; and the flow chart followed to calculate the breathing rate (PDF)

AUTHOR INFORMATION

Corresponding Authors

Boby George − *Department of Electrical Engineering, Indian Institute of Technology, Chennai 600036, India*; Email: boby@iitm.ac.in

Thalappil Pradeep − *DST Unit of Nanoscience and Thematic Unit of Excellence, Department of Chemistry, Indian Institute of Technology, Chennai 600036, India; International Centre for Clean Water, IIT Madras Research Park, Chennai 600113, India*; orcid.org/0000-0003-3174-534X; Email: pradeep@iitm.ac.in

Authors

Pillalamarri Srikrishnarka − *DST Unit of Nanoscience and Thematic Unit of Excellence, Department of Chemistry, Indian Institute of Technology, Chennai 600036, India*; *Department of Chemical Engineering, Indian Institute of Technology, Chennai 600036, India*; orcid.org/0000-0001-5187-6879

Raaga Madhuri Dasi − *Department of Electrical Engineering, Indian Institute of Technology, Chennai 600036, India*; orcid.org/0000-0002-1166-318X

Sourav Kanti Jana − *DST Unit of Nanoscience and Thematic Unit of Excellence, Department of Chemistry, Indian Institute of Technology, Chennai 600036, India*; orcid.org/0000-0001-5772-7022

Tripti Ahuja − *DST Unit of Nanoscience and Thematic Unit of Excellence, Department of Chemistry, Indian Institute of Technology, Chennai 600036, India*

Jenifer Shantha Kumar − *DST Unit of Nanoscience and Thematic Unit of Excellence, Department of Chemistry, Indian Institute of Technology, Chennai 600036, India*

Ankit Nagar − *DST Unit of Nanoscience and Thematic Unit of Excellence, Department of Chemistry, Indian Institute of Technology, Chennai 600036, India*

Amoghavarsha Ramachandra Kini − *DST Unit of Nanoscience and Thematic Unit of Excellence, Department of Chemistry, Indian Institute of Technology, Chennai 600036, India*

Complete contact information is available at: https://pubs.acs.org/10.1021/acsomega.2c05017

Author Contributions

P.S. and R.M.D. contributed equally to this work. T.P. designed the problem, and P.S. optimized the sensor and characterized it. Electrochemical testing of the sensor was performed by S.K.J., R.M.D. designed the circuit and the Android application, which was evaluated by B.G.. T.A. performed the time-dependent Raman studies, and AK assisted with the figures. S.K.J. performed the antibacterial studies. All authors contributed to the writing of the manuscript.

Notes

The authors declare no competing financial interest.
Code will be provided upon request from the authors.

ACKNOWLEDGMENTS

The authors thank the Department of Science and Technology, Government of India, for supporting our research on nanomaterials. P.S., S.K.J., T.A., A.N., and S.K.J. thank IIT Madras for their research fellowship. AK thanks the Council of Science and Industrial Research (CSIR), Government of India, for a research fellowship. The authors acknowledge Professor Pijush Ghosh, Department of Applied Mechanics, IIT Madras, for helping them with contact angle measurements. They also thank all volunteers for their participation in this study, Dr. Premkumar for his assistance in presenting the sensing mechanism, and Dr. Joseph G. Manion of CG Figures for providing blender files needed for making the beakers.

REFERENCES

(1) Soriano, J. B.; Kendrick, P. J.; Paulson, K. R.; Gupta, V.; Abrams, E. M.; Adedoyin, R. A.; Adhikari, T. B.; Advani, S. M.; Agrawal, A.; Ahmadian, E.; Alahdab, F.; Aljunid, S. M.; Altirkawi, K. A.; Alvis-Guzman, N.; Anber, N. H.; Andrei, C. L.; Anjomshoa, M.; Ansari, F.; Antó, J. M.; Arabloo, J.; Athari, S. M.; Athari, S. S.; Awoke, N.; Badawi, A.; Banoub, J. A. M.; Bennett, D. A.; Bensenor, I. M.; Berfield, K. S. S.; Bernstein, R. S.; Bhattacharyya, K.; Bijani, A.; Brauer, M.; Bukhman, G.; Butt, Z. A.; Cámera, L. A.; Car, J.; Carrero, J. J.; Carvalho, F.; Castañeda-Orjuela, C. A.; Choi, J.-Y. J.;

https://doi.org/10.1021/acsomega.2c05017
ACS Omega 2022, 7, 42926−42938

Christopher, D. J.; Cohen, A. J.; Dandona, L.; Dandona, R.; Dang, A. K.; Daryani, A.; Courten, B.; de Demeke, F. M.; Demoz, G. T.; Neve, J.-W. D.; Desai, R.; Dharmaratne, S. D.; Diaz, D.; Douiri, A.; Driscoll, T. R.; Duken, E. E.; Eftekhari, A.; Elkout, H.; Endries, A. Y.; Fadhil, I.; Faro, A.; Farzadfar, F.; Fernandes, E.; Filip, I.; Fischer, F.; Foroutan, M.; Garcia-Gordillo, M. A.; Gebre, A. K.; Gebremedhin, K. B.; Gebremeskel, G. G.; Gezae, K. E.; Ghoshal, A. G.; Gill, P. S.; Gillum, R. F.; Goudarzi, H.; Guo, Y.; Gupta, R.; Hailu, G. B.; Hasanzadeh, A.; Hassen, H. Y.; Hay, S. I.; Hoang, C. L.; Hole, M. K.; Horita, N.; Hosgood, H. D.; Hostiuc, M.; Househ, M.; Ilesanmi, O. S.; Ilic, M. D.; Irvani, S. S. N.; Islam, S. M. S.; Jakovljevic, M.; Jamal, A. A.; Jha, R. P.; Jonas, J. B.; Kabir, Z.; Kasaeian, A.; Kasahun, G. G.; Kassa, G. M.; Kefale, A. T.; Kengne, A. P.; Khader, Y. S.; Khafaie, M. A.; Khan, E. A.; Khan, J.; Khubchandani, J.; Kim, Y.-E.; Kim, Y. J.; Kisa, S.; Kisa, A.; Knibbs, L. D.; Komaki, H.; Koul, P. A.; Koyanagi, A.; Kumar, G. A.; Lan, Q.; Lasrado, S.; Lauriola, P.; Vecchia, C. L.; Le, T. T.; Leigh, J.; Levi, M.; Li, S.; Lopez, A. D.; Lotufo, P. A.; Madotto, F.; Mahotra, N. B.; Majdan, M.; Majeed, A.; Malekzadeh, R.; Mamun, A. A.; Manafi, N.; Manafi, F.; Mantovani, L. G.; Meharie, B. G.; Meles, H. G.; Meles, G. G.; Menezes, R. G.; Mestrovic, T.; Miller, T. R.; Mini, G. K.; Mirrakhimov, E. M.; Moazen, B.; Mohammad, K. A.; Mohammed, S.; Mohebi, F.; Mokdad, A. H.; Molokhia, M.; Monasta, L.; Moradi, M.; Moradi, G.; Morawska, L.; Mousavi, S. M.; Musa, K. I.; Mustafa, G.; Naderi, M.; Naghavi, M.; Naik, G.; Nair, S.; Nangia, V.; Nansseu, J. R.; Nazari, J.; Ndwandwe, D. E.; Negoi, R. I.; Nguyen, T. H.; Nguyen, C. T.; Nguyen, H. L. T.; Nixon, M. R.; Ofori-Asenso, R.; Ogbo, F. A.; Olagunju, A. T.; Olagunju, T. O.; Oren, E.; Ortiz, J. R.; Owolabi, M. O.; A, M. P.; Pakhale, S.; Pana, A.; Panda-Jonas, S.; Park, E.-K.; Pham, H. Q.; Postma, M. J.; Pourjafar, H.; Poustchi, H.; Radfar, A.; Rafiei, A.; Rahim, F.; Rahman, M. H. U.; Rahman, M. A.; Rawaf, S.; Rawaf, D. L.; Rawal, L.; R, C. R., Jr; Reitsma, M. B.; Roever, L.; Ronfani, L.; Roro, E. M.; Roshandel, G.; Rudd, K. E.; Sabde, Y. D.; Sabour, S.; Saddik, B.; Safari, S.; Saleem, K.; Samy, A. M.; Santric-Milicevic, M. M.; Jose, B. P. S.; Sartorius, B.; Satpathy, M.; Savic, M.; Sawhney, M.; Sepanlou, S. G.; Shaikh, M. A.; Sheikh, A.; Shigematsu, M.; Shirkoohi, R.; Si, S.; Siabani, S.; Singh, V.; Singh, J. A.; Soljak, M.; Somayaji, R.; Soofi, M.; Soyiri, I. N.; Tefera, Y. M.; Temsah, M.-H.; Tesfay, B. E.; Thakur, J. S.; Toma, A. T.; Tortajada-Girbés, M.; Tran, K. B.; Tran, B. X.; Car, L. T.; Ullah, I.; Vacante, M.; Valdez, P. R.; Boven, J. F. M. van.; Vasankari, T. J.; Veisani, Y.; Violante, F. S.; Wagner, G. R.; Westerman, R.; Wolfe, C. D. A.; Wondafrash, D. Z.; Wondmieneh, A. B.; Yonemoto, N.; Yoon, S.-J.; Zaidi, Z.; Zamani, M.; Zar, H. J.; Zhang, Y.; Vos, T. Prevalence and Attributable Health Burden of Chronic Respiratory Diseases, 1990−2017: A Systematic Analysis for the Global Burden of Disease Study 2017. *Lancet Respir. Med.* **2020**, *8*, 585−596.

(2) Wyrwa, J.; Barska, A. Innovations in the Food Packaging Market: Active Packaging. *Eur. Food Res. Technol.* **2017**, *243*, 1681−1692.

(3) Benabdellah, N.; Bourhaleb, M.; Nasri, M.; Benazzi, N.; Dahbi, S. In *Design of Temperature and Humidity Sensors for an Electronic Nose Used in Rotten Food*, International Conference on Electrical and Information Technologies (ICEIT), 2016.

(4) Brown, M. E.; de Beurs, K. M.; Marshall, M. Global Phenological Response to Climate Change in Crop Areas Using Satellite Remote Sensing of Vegetation, Humidity and Temperature over 26years. *Remote Sens. Environ.* **2012**, *126*, 174−183.

(5) Popov, T. A. Human Exhaled Breath Analysis. *Ann. Allergy, Asthma, Immunol.* **2011**, *106*, 451−456.

(6) Das, S.; Pal, M. Review—Non-Invasive Monitoring of Human Health by Exhaled Breath Analysis: A Comprehensive Review. *J. Electrochem. Soc.* **2020**, *167*, No. 037562.

(7) Kim, Y.; Jung, B.; Lee, H.; Kim, H.; Lee, K.; Park, H. Capacitive Humidity Sensor Design Based on Anodic Aluminum Oxide. *Sens. Actuators, B* **2009**, *141*, 441−446.

(8) Zampetti, E.; Pantalei, S.; Pecora, A.; Valletta, A.; Maiolo, L.; Minotti, A.; Macagnano, A.; Fortunato, G.; Bearzotti, A. Design and Optimization of an Ultra Thin Flexible Capacitive Humidity Sensor. *Sens. Actuators, B* **2009**, *143*, 302−307.

(9) Hijikagawa, M.; Miyoshi, S.; Sugihara, T.; Jinda, A. A Thin-Film Resistance Humidity Sensor. *Sens. Actuators* **1983**, *4*, 307−315.

(10) Yi, Y.; Jiang, Y.; Zhao, H.; Brambilla, G.; Fan, Y.; Wang, P. High-Performance Ultrafast Humidity Sensor Based on Microknot Resonator-Assisted Mach−Zehnder for Monitoring Human Breath. *ACS Sens.* **2020**, *5*, 3404−3410.

(11) Zhao, Z.; Duan, Y. A Low Cost Fiber-Optic Humidity Sensor Based on Silica Sol−Gel Film. *Sens. Actuators, B* **2011**, *160*, 1340−1345.

(12) Ando, M.; Kobayashi, T.; Haruta, M. Humidity-Sensitive Optical Absorption of Co3O4 Film. *Sens. Actuators, B* **1996**, *32*, 157−160.

(13) Hashim, A.; Hadi, A. Synthesis and Characterization of (MgO−Y2O3−CuO) Nanocomposites for Novel Humidity Sensor Application. *Sens. Lett.* **2017**, *15*, 858−861.

(14) Wu, J.; Yin, C.; Zhou, J.; Li, H.; Liu, Y.; Shen, Y.; Garner, S.; Fu, Y.; Duan, H. Ultrathin Glass-Based Flexible, Transparent, and Ultrasensitive Surface Acoustic Wave Humidity Sensor with ZnO Nanowires and Graphene Quantum Dots. *ACS Appl. Mater. Interfaces* **2020**, *12*, 39817−39825.

(15) Sheng, L.; Dajing, C.; Yuquan, C. A Surface Acoustic Wave Humidity Sensor with High Sensitivity Based on Electrospun MWCNT/Nafion Nanofiber Films. *Nanotechnology* **2011**, *22*, No. 265504.

(16) Caliendo, C.; Verona, E.; D'Amico, A.; Furlani, A.; Iucci, G.; Russo, M. V. Surface Acoustic Wave Humidity Sensor. *Sens. Actuators, B* **1993**, *16*, 288−292.

(17) Penza, M.; Anisimkin, V. I. Surface Acoustic Wave Humidity Sensor Using Polyvinyl-Alcohol Film. *Sens. Actuators, A* **1999**, *76*, 162−166.

(18) Chen, Q.; Feng, N.; Huang, X.; Yao, Y.; Jin, Y.; Pan, W.; Liu, D. Humidity-Sensing Properties of a BiOCl-Coated Quartz Crystal Microbalance. *ACS Omega* **2020**, *5*, 18818−18825.

(19) Qi, P.; Xu, Z.; Zhang, T.; Fei, T.; Wang, R. Chitosan Wrapped Multiwalled Carbon Nanotubes as Quartz Crystal Microbalance Sensing Material for Humidity Detection. *J. Colloid Interface Sci.* **2020**, *560*, 284−292.

(20) Tang, L.; Chen, W.; Chen, B.; Lv, R.; Zheng, X.; Rong, C.; Lu, B.; Huang, B. Sensitive and Renewable Quartz Crystal Microbalance Humidity Sensor Based on Nitrocellulose Nanocrystals. *Sens. Actuators, B* **2021**, *327*, No. 128944.

(21) Pascal-Delannoy, F.; Sorli, B.; Boyer, A. Quartz Crystal Microbalance (QCM) Used as Humidity Sensor. *Sens. Actuators Phys.* **2000**, *84*, 285−291.

(22) Wu, S.; Wang, G.; Xue, Z.; Ge, F.; Zhang, G.; Lu, H.; Qiu, L. Organic Field-Effect Transistors with Macroporous Semiconductor Films as High-Performance Humidity Sensors. *ACS Appl. Mater. Interfaces* **2017**, *9*, 14974−14982.

(23) Song, S.-H.; Yang, H.-H.; Han, C.-H.; Ko, S.-D.; Lee, S.-H.; Yoon, J.-B. Metal-Oxide-Semiconductor Field Effect Transistor Humidity Sensor Using Surface Conductance. *Appl. Phys. Lett.* **2012**, *100*, No. 101603.

(24) Mogera, U.; Sagade, A. A.; George, S. J.; Kulkarni, G. U. Ultrafast Response Humidity Sensor Using Supramolecular Nanofibre and Its Application in Monitoring Breath Humidity and Flow. *Sci. Rep.* **2014**, *4*, No. 4103.

(25) Lin, Q.; Li, Y.; Yang, M. Highly Sensitive and Ultrafast Response Surface Acoustic Wave Humidity Sensor Based on Electrospun Polyaniline/Poly(Vinyl Butyral) Nanofibers. *Anal. Chim. Acta* **2012**, *748*, 73−80.

(26) Güder, F.; Anila, A.; Redson, J.; Mosadegh, B.; Glavan, A.; Martin, T. J.; Whitesides, G. M. Paper-Based Electrical Respiration Sensor. *Angew. Chem., Int. Ed.* **2016**, *55*, 5727−5732.

(27) Duan, Z.; Jiang, Y.; Yan, M.; Wang, S.; Yuan, Z.; Zhao, Q.; Sun, P.; Xie, G.; Du, X.; Tai, H. Facile, Flexible, Cost-Saving, and Environment-Friendly Paper-Based Humidity Sensor for Multifunctional Applications. *ACS Appl. Mater. Interfaces* **2019**, *11*, 21840−21849.

https://doi.org/10.1021/acsomega.2c05017
ACS Omega 2022, 7, 42926−42938

(28) Guan, X.; Hou, Z.; Wu, K.; Zhao, H.; Liu, S.; Fei, T.; Zhang, T. Flexible Humidity Sensor Based on Modified Cellulose Paper. *Sens. Actuators, B* **2021**, *339*, No. 129879.
(29) Zhu, P.; Ou, H.; Kuang, Y.; Hao, L.; Diao, J.; Chen, G. Cellulose Nanofiber/Carbon Nanotube Dual Network-Enabled Humidity Sensor with High Sensitivity and Durability. *ACS Appl. Mater. Interfaces* **2020**, *12*, 33229−33238.
(30) Wang, Y.; Zhang, L.; Zhou, J.; Lu, A. Flexible and Transparent Cellulose-Based Ionic Film as a Humidity Sensor. *ACS Appl. Mater. Interfaces* **2020**, *12*, 7631−7638.
(31) Zhao, H.; Zhang, T.; Qi, R.; Dai, J.; Liu, S.; Fei, T. Drawn on Paper: A Reproducible Humidity Sensitive Device by Handwriting. *ACS Appl. Mater. Interfaces* **2017**, *9*, 28002−28009.
(32) Zhu, P.; Kuang, Y.; Wei, Y.; Li, F.; Ou, H.; Jiang, F.; Chen, G. Electrostatic Self-Assembly Enabled Flexible Paper-Based Humidity Sensor with High Sensitivity and Superior Durability. *Chem. Eng. J.* **2021**, *404*, No. 127105.
(33) Zhang, X.; He, D.; Yang, Q.; Atashbar, M. Z. Rapid, Highly Sensitive, and Highly Repeatable Printed Porous Paper Humidity Sensor. *Chem. Eng. J.* **2022**, *433*, No. 133751.
(34) Chen, X.; Li, Y.; Wang, X.; Yu, H. Origami Paper-Based Stretchable Humidity Sensor for Textile-Attachable Wearable Electronics. *ACS Appl. Mater. Interfaces* **2022**, *14*, 36227−36237.
(35) Li, X.; Guo, Y.; Meng, J.; Li, X.; Li, M.; Gao, D. Self-Powered Carbon Ink/Filter Paper Flexible Humidity Sensor Based on Moisture-Induced Voltage Generation. *Langmuir* **2022**, *38*, 8232−8240.
(36) Ismar, E.; Kurşun Bahadir, S.; Kalaoglu, F.; Koncar, V. Futuristic Clothes: Electronic Textiles and Wearable Technologies. *Global Challenges* **2020**, *4*, No. 1900092.
(37) Ma, C.; Yuan, Q.; Du, H.; Ma, M.-G.; Si, C.; Wan, P. Multiresponsive MXene (Ti3C2Tx)-Decorated Textiles for Wearable Thermal Management and Human Motion Monitoring. *ACS Appl. Mater. Interfaces* **2020**, *12*, 34226−34234.
(38) Wu, J.; Wang, Z.; Liu, W.; Wang, L.; Xu, F. Bioinspired Superelastic Electroconductive Fiber for Wearable Electronics. *ACS Appl. Mater. Interfaces* **2019**, *11*, 44735−44741.
(39) Wang, Y.; Zhang, L.; Zhang, Z.; Sun, P.; Chen, H. High-Sensitivity Wearable and Flexible Humidity Sensor Based on Graphene Oxide/Non-Woven Fabric for Respiration Monitoring. *Langmuir* **2020**, *36*, 9443−9448.
(40) Allison, L. K.; Rostaminia, S.; Kiaghadi, A.; Ganesan, D.; Andrew, T. L. Enabling Longitudinal Respiration Monitoring Using Vapor-Coated Conducting Textiles. *ACS Omega* **2021**, *6*, 31869−31875.
(41) Xie, R.; Du, Q.; Zou, B.; Chen, Y.; Zhang, K.; Liu, Y.; Liang, J.; Zheng, B.; Li, S.; Zhang, W.; Wu, J.; Huo, F. Wearable Leather-Based Electronics for Respiration Monitoring. *ACS Appl. Bio Mater.* **2019**, *2*, 1427−1431.
(42) Rauf, S.; Vijjapu, M. T.; Andrés, M. A.; Gascón, I.; Roubeau, O.; Eddaoudi, M.; Salama, K. N. Highly Selective Metal−Organic Framework Textile Humidity Sensor. *ACS Appl. Mater. Interfaces* **2020**, *12*, 29999−30006.
(43) Bokka, N.; Karhade, J.; Sahatiya, P. Deep Learning Enabled Classification of Real-Time Respiration Signals Acquired by MoSSe Quantum Dot-Based Flexible Sensors. *J. Mater. Chem. B* **2021**, *9*, 6870−6880.
(44) Liu, L.; Ni, Y.; Mao, J.; Li, S.; Ng, K. H.; Chen, Z.; Huang, J.; Cai, W.; Lai, Y. Flexible and Highly Conductive Textiles Induced by Click Chemistry for Sensitive Motion and Humidity Monitoring. *ACS Appl. Mater. Interfaces* **2022**, *14*, 37878−37886.
(45) Iyengar, S. A.; Srikrishnarka, P.; Jana, S. K.; Islam, M. R.; Ahuja, T.; Mohanty, J. S.; Pradeep, T. Surface-Treated Nanofibers as High Current Yielding Breath Humidity Sensors for Wearable Electronics. *ACS Appl. Electron. Mater.* **2019**, *1*, 951−960.
(46) Tanda, N.; Hinokio, Y.; Washio, J.; Takahashi, N.; Koseki, T. Breath Acetone in Type 1 and Type 2 Diabetes Mellitus. In *Interface Oral Health Science 2011*; Sasaki, K.; Suzuki, O.; Takahashi, N., Eds.; Springer Japan: Tokyo, 2012; pp 212−214.
(47) Wu, L.; McIntosh, M.; Zhang, X.; Ju, H. Amperometric Sensor for Ethanol Based on One-Step Electropolymerization of Thionine-Carbon Nanofiber Nanocomposite Containing Alcohol Oxidase. *Talanta* **2007**, *74*, 387−392.
(48) Liu, C.; Bonaccurso, E.; Butt, H.-J. Evaporation of Sessile Water/Ethanol Drops in a Controlled Environment. *Phys. Chem. Chem. Phys.* **2008**, *10*, 7150−7157.
(49) Farahani, H.; Wagiran, R.; Hamidon, M. Humidity Sensors Principle, Mechanism, and Fabrication Technologies: A Comprehensive Review. *Sensors* **2014**, *14*, 7881−7939.

https://doi.org/10.1021/acsomega.2c05017
ACS Omega 2022, 7, 42926−42938